Journal of Computational Physics 228 (2009) 4789–4810

Contents lists available at ScienceDirect

Journal of Computational Physics

journal homepage: www.elsevier.com/locate/jcp

An efficient three-dimensional adaptive quasicontinuum method using variable-node elements

Sungjin Kwon [a], Youngmin Lee [a], Jong Youn Park [b], Dongwoo Sohn [a], Jae Hyuk Lim [c], Seyoung Im [a,*]

[a] Department of Mechanical Engineering, Korea Advanced Institute of Science and Technology (KAIST), Science Town, Daejeon 305-701, Republic of Korea
[b] Technical Research Lab., POSCO, Pohang, Gyeongbuk, Republic of Korea
[c] Satellite Structure Department, Korea Aerospace Research Institute, 115 Gwahangno 45, Eoeun-dong, Yuseong-gu, Daejeon 305-333, Republic of Korea

ARTICLE INFO

Article history:
Received 3 December 2008
Received in revised form 2 March 2009
Accepted 23 March 2009
Available online 31 March 2009

Keywords:
Qasicontinuum
Variable-node elements
Multiscale modeling
Nanoindentation
Adaptive mesh refinement

ABSTRACT

A new quasicontinuum (QC) implementation using the so-called "variable-node finite elements" is reported in this work. Tetrahedral elements, which have been exclusively utilized for the conventional QC are replaced by hexahedral elements in conjunction with the so-called variable-node elements. This enables an effective adaptive mesh refinement in QC, leading to fast and efficient simulations compared with the conventional QC. To confirm the solution accuracy, comparison is made for a nanoindentation problem with a molecular dynamics simulation as well as a molecular mechanics solution. Further examples of nanoindentation are shown and discussed to demonstrate the effectiveness of the present scheme.

1. Introduction

The limitations of spatial and temporal scales are well known characteristics of atomistic simulation. To overcome these limitations, various multiscale simulation methods that is capable of bridging different scales have been explored; to name a few, for example, but not limited to, the references [1–10]. Among others, the quasicontinuum (QC) method [5–10] is one of the most successful multiscale simulation methods. It allocates the full atomic degrees of freedom for the domain called the nonlocal region, where defects occur, such as voids, dislocations or twins etc. On the other hand, for the local region, where deformations are relatively mild enough to be dictated by the Cauchy–Born rule, a smaller number of degrees of freedom are allocated through coarse-graining.

Since the QC was first reported by Tadmor et al. [5], the behaviors of various defects and their interactions, such as, cracks, dislocations, grain boundaries and so on, have been successfully studied with the aid of this method [5–10]. The QC method may be categorized into two approaches. The first, known as local QC, is formulated in the continuum-like finite element framework [5,6]. The local QC is not capable of dealing with the full atomistic details taking place at the atomic-level description such as dislocation cores, stacking faults and grain boundaries. The second is the nonlocal QC, in which the energy of the system is calculated from the atomistic potential [6,8]. In the mixed approach wherein the local QC is combined with the

* Corresponding author. Tel.: +82 42 350 3028; fax: +82 42 350 3210.
E-mail address: sim@kaist.ac.kr (S. Im).
URL: http://mpsl.kaist.ac.kr (S. Im).

0021-9991/$ - see front matter © 2009 Elsevier Inc. All rights reserved.
doi:10.1016/j.jcp.2009.03.028

nonlocal QC, there may occur the so-called ghost force at the interface of the local QC and the nonlocal QC due to the inconsistency of energy approximation between the two methods.

The nonlocal QC is formulated in two different ways of expressing the energy of the system: the node-based formulation and the cluster summation [8]. In the fully nonlocal QC, the zero energy modes may occur when the node-based summation rule is employed. To eliminate the zero energy modes, Knap and Ortiz [8] introduced the so-called "cluster summation rule" as a fully nonlocal QC. This method paves the way to a seamless coupling of the two length scales between the atomistic and the continuum regions.

Among the key ingredients of the QC is an effective adaptive meshing scheme that controls the sizes of the individual element subdomains in an adaptive manner, consistent with the severity of the deformation. This scheme enables one to reach optimal meshing or coarsening so that a high resolution, very often down to the atomic-scale, may be obtained in regions of a stiff gradient of deformation, while appropriate reduction of the degrees of freedom may be accomplished in regions of relatively uniform deformation. The element refinement or coarsening depends on the severity of deformation, which is scarcely known a priori in many nanomechanics problems. In QC applications for such complex problems, accordingly, an adaptive meshing or refinement scheme is essential for an efficient and accurate solution. In the conventional QC method, most of the adaptive refinement is implemented by use of linear triangular or tetrahedral finite elements. This is due to the fact that adaptive refinement or meshing is achieved most readily through triangulation for triangular or tetrahedral finite elements. Despite the high geometric adaptability of triangular or tetrahedral elements, these elements are far from being satisfactory in terms of the solution accuracy and overall efficiency. It is well known in computational mechanics that the performance of the hexahedral type element is better than that of the tetrahedral type element. Therefore, a QC implemented with the hexahedral type elements may be more efficient. Elements having large aspect ratios may be found in tetrahedral finite element meshes of complex geometry. In this case, they are usually the source of a substantial error as the nodal points are not appropriate for the sampling points for representing the behaviors of the material points in those element domains. In the same context, the nodal points of a tetrahedral QC element having a large aspect ratio are not suitable for the sampling points to represent the overall deformation behaviors of the atoms contained in the element. To construct a desirable adaptive mesh by preventing large aspect ratios, in general a mesh generation code for the constrained Delaunay triangulation is incorporated into the conventional QC with tetrahedral elements [11].

In terms of the availability of an efficient alternative, what are known as variable-node elements [12–18] are a powerful tool for adaptive refinement. In this context, it is not necessary to use only triangular or tetrahedral elements for the implementation of the QC. The QC with hexahedral elements in conjunction with the variable-node elements is capable of refining elements without any additional programs for mesh generation; no Delaunay triangulation is needed, as opposed to the QC with tetrahedral elements. In addition, aspect ratios of elements in the course of refinement are well controlled in the QC with hexahedral elements combined with variable-node elements.

In this study, presented is a new implementation for the fully nonlocal QC, replacing tetrahedral elements used in the conventional QC by the hexahedral elements. For an efficient adaptive mesh refinement, the variable-node elements [12–18] are employed to bridge concurrently between different scales of meshes. To test the performance of the present QC with hexahedral elements in conjunction with the variable-node elements, nanoindentation [19–31] simulations are conducted under various conditions. Comparison is made to the conventional QC in terms of the effectiveness. In addition, employing the present QC simulation for nanoindentation, we explore the onset of dislocations, followed by the subsequent development and the interaction of some defects.

The outline of the paper is as follows. In Section 2, the fully nonlocal QC and the variable-node elements are described and this is followed by adaptive meshing refinement in Section 3 and numerical examples in Section 4. Finally, Section 5 closes the paper with some concluding remarks.

2. New implementation of the QC with the hexahedral type elements

In this section, the formulation of the fully nonlocal QC is briefly described and the key notion of variable-node elements is summarized. This is followed by our discussion on how to construct the overall scheme for an adaptive QC simulation by use of variable-node elements.

2.1. The overview of the nonlocal QC based on cluster-based summation

Knap and Ortiz [8] proposed the fully nonlocal QC based on the cluster summation rule. This nonlocal QC requires more computations compared to the local QC, which is based on the notion of the locally homogeneous deformations in continuum. The local QC therefore assumes the validity of the Cauchy–Born rule and uses deformation gradient and strain variables based on continuum mechanics to link deformation to constitutive equations, which may be one derived from atomic potentials or one from a phenomenological continuum theory.

In the absence of external forces, the total energy E_{total} of a system is given as the summation of energy E_i for every atom:

$$E_{total} = \sum_{i=1}^{N} E_i \tag{1}$$

where N is the number of atoms in the system. There are two approaches of formulation for coarse-graining in the nonlocal QC method, named the energy-based method and the force-based method [6]. In the present work, the energy-based method is utilized and there are two methods of expressing the energy of the system in the nonlocal QC [8]. The first, known as the node-based summation rule, is to sum over each node or over the individual representative atom the energy associated with the individual node. The second approach is the cluster summation rule, which calculates the total energy as the summation of the cluster energy. Here the cluster is a collection of atoms within the cluster radius from a given node.

In the node-based summation rule, the total energy E_{total} can be expressed as the approximated total energy E^h_{total} using the energy of the representative atom E_α as follows:

$$E_{total} \approx E^h_{total} = \sum_{\alpha=1}^{N_R} w_\alpha E_\alpha \tag{2}$$

Here, N_R, α and w_α represent the total number of representative atoms, a node number for a representative atom and a weight function of representative atom α, respectively. The physical meaning of the weight function w_α is the number of ordinary atoms represented by a representative atom α [6]. In the QC method, we assume that the energy of an individual atom E_i is expressible through interpolation in terms of the energies E_α of the representative atoms:

$$E_i \approx E^h_i = \sum_{\alpha=1}^{N_R} H_\alpha(\mathbf{X}_i) E_\alpha \tag{3}$$

Here, $H_\alpha(\mathbf{X}_i)$ denotes a shape function in finite element method, and E^h_i and E_α the approximate energy of an individual atom and the energy of the representative atom at node α. The shape function $H_\alpha(\mathbf{X}_i)$ interpolates the current position of ordinary atoms using the mapping from a reference coordinate $\mathbf{X}_i$ to a current coordinate $\mathbf{x}_i$.

$$\mathbf{x}^h_i = \sum_{\alpha=1}^{N_R} H_\alpha(\mathbf{X}_i)\mathbf{x}_\alpha \tag{4}$$

From Eqs. (1) and (3), it follows that

$$E_{total} = \sum_{i=1}^{N}\sum_{\alpha=1}^{N_R} H_\alpha(\mathbf{X}_i) E_\alpha \tag{5}$$

Then, Eqs. (2) and (5) yield the weight function w_α in terms of the shape function $H_\alpha(\mathbf{X}_i)$:

$$w_\alpha = \sum_{i=1}^{N} H_\alpha(\mathbf{X}_i) \tag{6}$$

The above node-base summation rule may lead to zero energy modes [8], which may be avoided by choosing a sufficient number of representative atoms. Knap and Ortiz [8] proposed the cluster-based summation rule to resolve this problem in an effective manner. In this rule, the total energy of the system is not represented by the energy of the representative atoms but by the summation of the cluster energy E^c_β:

$$E^h_{total} = \sum_{\beta=1}^{N_R} w^c_\beta E^c_\beta = \sum_{\beta=1}^{N_R} w^c_\beta \left[\sum_{i\in cluster\beta} E_i\right] = \sum_{\beta=1}^{N_R} w^c_\beta \left[\sum_{i\in cluster\beta}\sum_{\alpha=1}^{N_R} H_\alpha(\mathbf{X}_i) E_\alpha\right] \tag{7}$$

Here, the cluster weight w^c_β is obtained from Eqs. (5) and (7) as

$$w_\alpha = \sum_{\beta=1}^{N_R} w^c_\beta \left[\sum_{i\in cluster\beta} H_\alpha(\mathbf{X}_i)\right] \tag{8}$$

The solution to this system of N_R equations yields the cluster weight function w^c_β. In the solution procedure, an efficient approximation may be made by replacing the coefficient matrix with a diagonal matrix by way of a "lumping process" based on the row-sum technique. This replaces the diagonal entries by summation of all entries on the corresponding rows, leaving all off-diagonal entries zero (see p. 444 of [32]). The decoupling due to this diagonalization renders the solution process for this system of linear equations trivial. Note that this technique is widely used for lumping mass matrices in dynamic finite element equations.

2.2. Variable-node elements for QC method

In the conventional QC method, triangular and tetrahedral elements are employed for the coarse-graining of a two- and a three-dimensional domain, respectively. However, it is well known that quadrilateral or hexahedral elements show much better performance than triangular or tetrahedral elements in finite element methods. Nevertheless, the conventional QC method has adopted triangular or tetrahedral elements for convenience of adaptive refinement. That is, despite the better performance of quadrilateral and hexahedral elements, they are not commonly used in finite element simulations involving

adaptive refinement as in the QC method, whereas triangular and tetrahedral elements are frequently employed in this case. This is due to the fact that realizing the adaptive refinement for a mesh comprised of quadrilateral or hexahedral elements is not straightforward.

Recently, Lim et al. [14–17] showed that "nonmatching meshes", are efficiently treated utilizing variable-node elements. Particularly, the adaptive refinement in the presence of quadrilateral or hexahedral elements was easily handled by variable-node elements. They have been successfully employed with regards to nonmatching problems and for bridging between two shape functions of different orders for smooth transition. This suggests that the use of variable-node elements may make it possible to utilize quadrilateral and hexahedral elements for more efficient QC implementation with adaptive refinement. The variable-node elements appear to violate the interelement compatibility according to the notion of the conventional finite elements. However, the nodal points are shared by the two neighboring elements and their shape functions are constructed such that the interelement compatibility is satisfied [15,18].

In this work, we employ hexahedral elements combined with three-dimensional variable-node elements in the QC for rectilinear crystalline materials. This enables one to implement the adaptive refinement for hexahedral elements in a straightforward manner, as the interelement compatibility is taken care of by the variable-node elements. Furthermore, an additional mesh generation program, which may be necessary for efficient refinement of triangular and tetrahedral elements, is not required for quadrilateral and hexahedral elements. The use of variable-node elements makes it possible to continue the adaptive refinement simply by adding elements and nodes where refinement is needed.

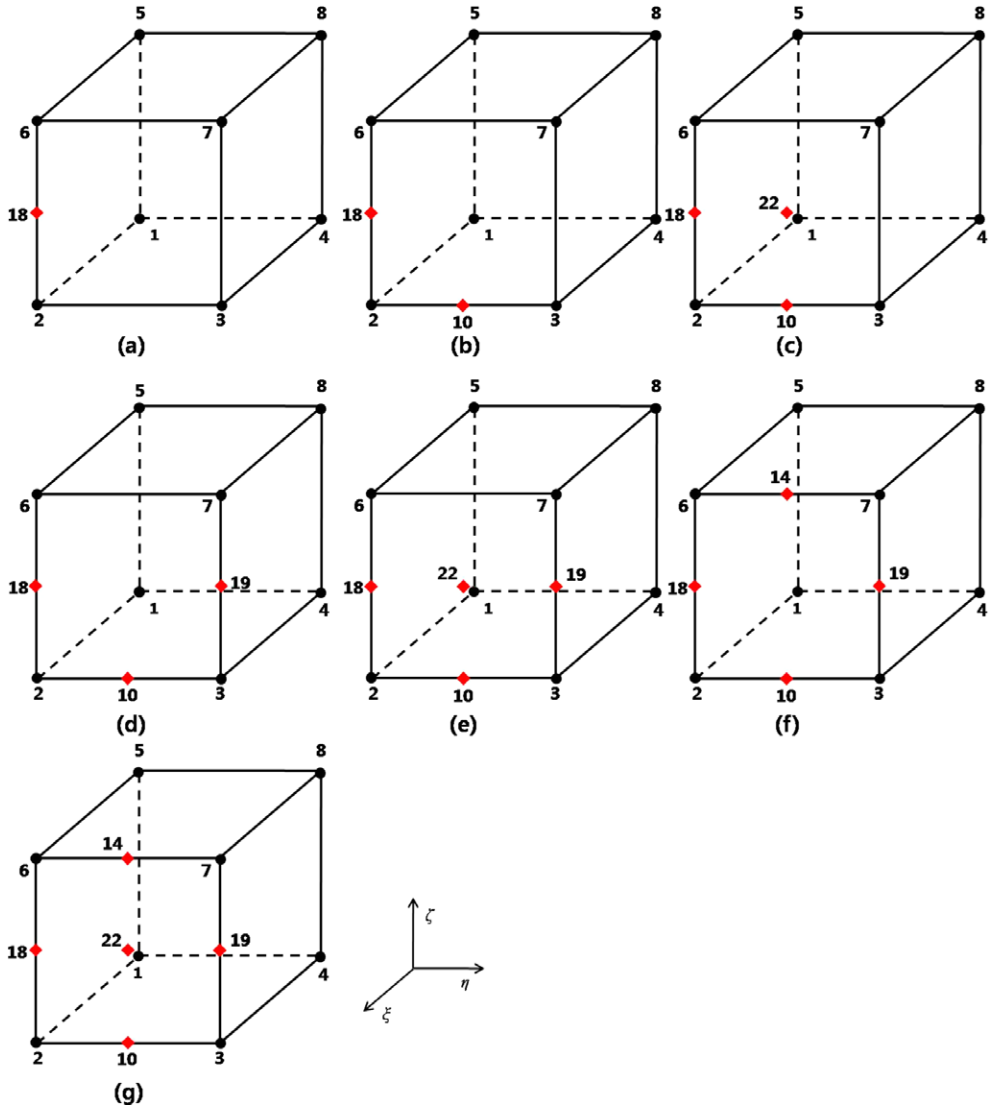

Fig. 1. Variable-node element with extra nodes on one face.

The three-dimensional variable-node elements introduced in this section are based on the hexahedral element with 8 nodes. The variable-node elements may have extra nodes up to 5 nodes on each face, which is allowed to be connected to one to four adjoined elements; for example, 1 to 5 nodes may be added only on one face so that 9 to 13-noded elements may be obtained (see Fig. 1). This addition of extra nodes may apply to some or all of the six faces; for example a 17-noded element may be obtained if two neighboring faces sharing one edge are provided with the full 9 extra nodes including one on the shared edge, or 16-noded elements are obtained if a set of any two opposite faces is chosen for the addition of the extra nodes only on the edges of the two faces with no nodes on the centers of the two faces. In case all faces are allowed to have the full extra nodes, obtained is the variable-node element with 26 nodes (see Fig. 2). Note that we do not have a node on the center of the variable-node element in Fig. 2, as the addition of the center node leads to the refinement into 8 hexahedral elements. According to the aforementioned description, the 8-noded hexahedral element may be thought of as a special case without any extra nodes in the context of the variable-node elements and so we write the present QC scheme as "the QC with variable-node elements".

Finite element shape functions are simply constructed by a hierarchical scheme in general. However, it is not straightforward to generate the shape functions of a three-dimensional variable-node element that have extra nodes on the edges or on the element faces. One may refer to the references [15] and [18] for detail on the construction of this element, which is briefly summarized here. For the construction of the shape functions of the variable-node elements, first we start with the shape functions for the regular 8-noded element $H_1^0 \sim H_8^0$.

$$H_i^0 = \frac{1}{8}(1+\xi\xi_i)(1+\eta\eta_i)(1+\zeta\zeta_i) \quad \text{for } i = 1,2,\ldots,8$$

In addition to these shape functions, we define the following shape functions for each of the extra nodes:

$$\begin{aligned}
H_i^0 &= \frac{1}{4}(1-|\xi|)(1+\eta\eta_i)(1+\zeta\zeta_i) \quad \text{for } i = 9,11,13,15 \text{ (odd number)} \\
H_i^0 &= \frac{1}{4}(1+\xi\xi_i)(1-|\eta|)(1+\zeta\zeta_i) \quad \text{for } i = 10,12,14,16 \text{ (even number)} \\
H_i^0 &= \frac{1}{4}(1+\xi\xi_i)(1+\eta\eta_i)(1-|\zeta|) \quad \text{for } i = 17,18,19,20 \\
H_i^0 &= \frac{1}{2}(1-|\xi|)(1+\eta\eta_i)(1-|\zeta|) \quad \text{for } i = 21,23 \\
H_i^0 &= \frac{1}{2}(1+\xi\xi_i)(1-|\eta|)(1-|\zeta|) \quad \text{for } i = 22,24 \\
H_i^0 &= \frac{1}{2}(1-|\xi|_i)(1-|\eta|)(1+\zeta\zeta_i) \quad \text{for } i = 25,26
\end{aligned} \tag{9}$$

Here, ξ, η and ζ indicate the coordinates of the master domain of the variable-node element in Fig. 2. Note that $H_i^0 (i = 9\text{–}20)$ indicates the shape function of node "i" when only node "i" is added at the center of an element edge. Furthermore, $H_i^0 (i = 21\text{–}26)$ denotes the shape function of node "i" when only "i" is added at the center of one of the four element faces.

The hierarchical subtraction is needed to construct the shape functions of a variable-node element to meet the Kronecker-delta condition in case more than one extra node is added. Consider the shape functions H_1—H_8; say H_i is now constructed by subtracting from H_i^0 the extra shape functions multiplied by the H_i^0 values at the node i. For example, consider the shape

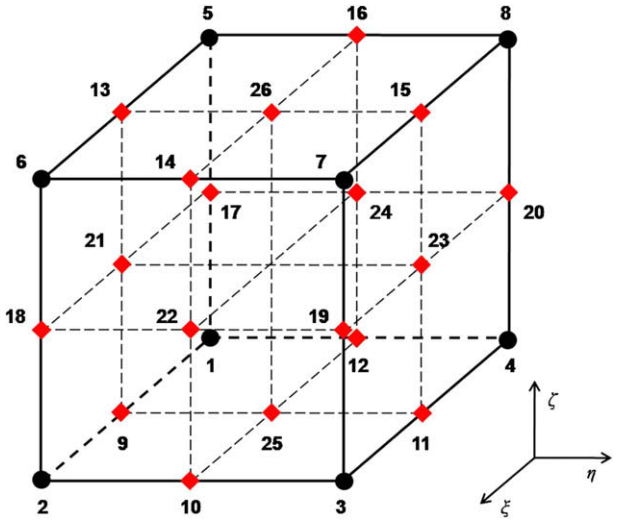

Fig. 2. The 26-noded hexahedral variable-node element with full extra nodes.

function H_2 of node 2 in case the extra nodes 9, 10 and 18 are added on the centers of the three edges (see Fig. 2). The shape function H_2 is expected to be zero at each of the extra nodes added, and this is made possible by adjusting H_2^0, which is not zero due to the additional nodes 9, 10 and 18. In addition to these 3 nodes and if nodes 21, 22 and 25 are added on the centers of the three faces, a similar hierarchical subtraction needs to be made. That is, for each of the extra nodes the original shape function H_2^0 is modified by hierarchically subtracting the extra shape functions multiplied by the values of H_2^0 at the nodes associated with the extra nodes. If all the extra nodes are inserted, the shape functions H_1 through H_8 are modified as follows:

$$\begin{aligned}
H_1 &= H_1^0 - \frac{1}{2}(H_9 + H_{12} + H_{17}) - \frac{1}{4}(H_{21} + H_{24} + H_{25}) \\
H_2 &= H_2^0 - \frac{1}{2}(H_9 + H_{10} + H_{18}) - \frac{1}{4}(H_{21} + H_{22} + H_{25}) \\
H_3 &= H_3^0 - \frac{1}{2}(H_{10} + H_{11} + H_{19}) - \frac{1}{4}(H_{22} + H_{23} + H_{25}) \\
H_4 &= H_4^0 - \frac{1}{2}(H_{11} + H_{12} + H_{20}) - \frac{1}{4}(H_{23} + H_{24} + H_{25}) \\
H_5 &= H_5^0 - \frac{1}{2}(H_{13} + H_{16} + H_{17}) - \frac{1}{4}(H_{21} + H_{24} + H_{26}) \\
H_6 &= H_6^0 - \frac{1}{2}(H_{13} + H_{14} + H_{18}) - \frac{1}{4}(H_{21} + H_{22} + H_{26}) \\
H_7 &= H_7^0 - \frac{1}{2}(H_{14} + H_{15} + H_{19}) - \frac{1}{4}(H_{22} + H_{23} + H_{26}) \\
H_8 &= H_8^0 - \frac{1}{2}(H_{15} + H_{16} + H_{20}) - \frac{1}{4}(H_{23} + H_{24} + H_{26})
\end{aligned} \tag{10}$$

Here, the shape functions $H_i (i = 21–26)$ are given as

$$H_i = H_i^0 \quad \text{for } i = 21, 22, \ldots, 26 \tag{11}$$

The remaining shape functions H_9–H_{20} are given by the followings:

$$\begin{aligned}
&H_i = H_i^0 - \frac{1}{2}(H_\alpha + H_\beta) \quad \text{for } i = 9, 10, \ldots, 20 \\
&\text{for } i = 9, 10, 11, 12: \quad \alpha = i + 12, \quad \beta = 25 \\
&\text{for } i = 13, 14, 15, 16: \quad \alpha = i + 8, \quad \beta = 26 \\
&\text{for } i = 17: \quad \alpha = 21, \quad \beta = 24 \\
&\text{for } i = 18, 19, 20: \quad \alpha = i + 3, \quad \beta = i + 4
\end{aligned} \tag{12}$$

where α and β are the node numbers for the nodes located at the center of two faces sharing the edge with mid-node i.

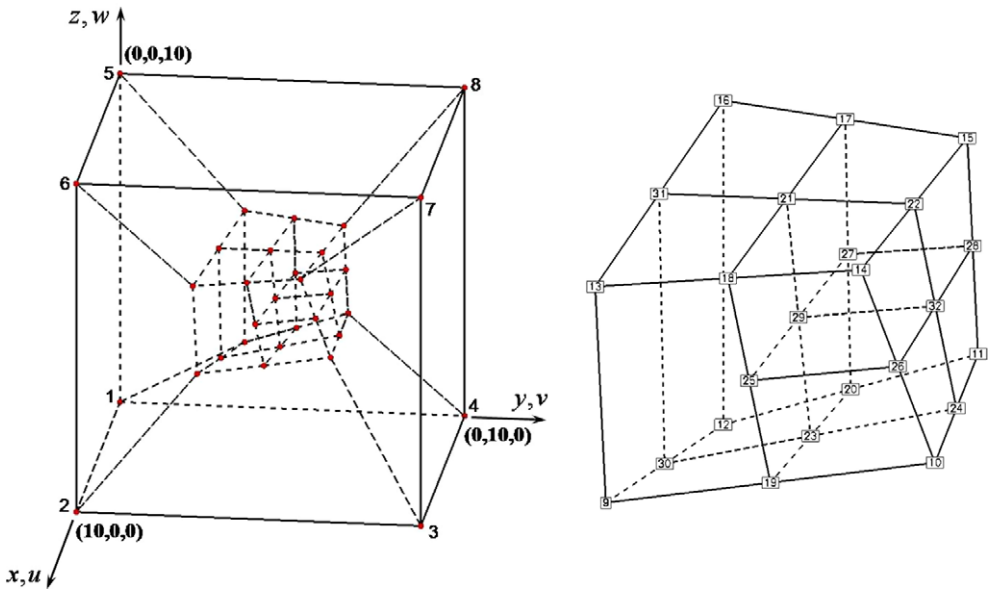

Fig. 3. Patch test model with variable-node elements for the linear displacement field: $u = \frac{1}{100}(3x + 2y + z)$, $v = \frac{1}{100}(x + 2y - z)$, $w = \frac{1}{100}(-2x + y + 4z)$, (left: full model, right: inner elements).

Table 1
The result of patch test; coordinates and displacements of the inner nodes.

Node	Coordinates of inner nodes			Exact displacements			Calculated displacements		
	x	y	z	u	v	w	u	v	w
9	6.0000	3.0000	3.0000	0.2700	0.0900	0.0300	0.2700	0.0900	0.0300
10	7.0000	7.0000	4.0000	0.3900	0.1700	0.0900	0.3900	0.1700	0.0900
11	3.0000	7.0000	4.0000	0.2700	0.1300	0.1700	0.2700	0.1300	0.1700
12	3.0000	4.0000	3.0000	0.2000	0.0800	0.1000	0.2000	0.0800	0.1000
13	7.0000	3.0000	6.0000	0.3300	0.0700	0.1300	0.3300	0.0700	0.1300
14	6.0000	6.0000	6.0000	0.3600	0.1200	0.1800	0.3600	0.1200	0.1800
15	4.0000	7.0000	7.0000	0.3300	0.1100	0.2700	0.3300	0.1100	0.2700
16	3.0000	4.0000	7.0000	0.2400	0.0400	0.2600	0.2400	0.0400	0.2600
17	3.5000	5.5000	7.0000	0.2850	0.0750	0.2650	0.2850	0.0750	0.2650
18	6.5000	4.5000	6.0000	0.3450	0.0950	0.1550	0.3450	0.0950	0.1550
19	6.5000	5.0000	3.5000	0.3300	0.1300	0.0600	0.3300	0.1300	0.0600
20	3.0000	5.5000	3.5000	0.2350	0.1050	0.1350	0.2350	0.1050	0.1350
21	5.0000	5.0000	6.5000	0.3150	0.0850	0.2100	0.3150	0.0850	0.2100
22	5.0000	6.5000	6.5000	0.3450	0.1150	0.2250	0.3450	0.1150	0.2250
23	4.7500	5.2500	3.5000	0.2825	0.1175	0.0975	0.2825	0.1175	0.0975
24	5.0000	7.0000	4.0000	0.3300	0.1500	0.1300	0.3300	0.1500	0.1300
25	6.5000	4.7500	4.7500	0.3375	0.1125	0.1075	0.3375	0.1125	0.1075
26	6.5000	6.5000	5.0000	0.3750	0.1450	0.1350	0.3750	0.1450	0.1350
27	3.2500	5.5000	5.2500	0.2600	0.0900	0.2000	0.2600	0.0900	0.2000
28	3.5000	7.0000	5.5000	0.3000	0.1200	0.2200	0.3000	0.1200	0.2200
29	4.8750	5.1250	5.0000	0.2988	0.1013	0.1538	0.2988	0.1013	0.1538
30	4.5000	3.5000	3.0000	0.2350	0.0850	0.0650	0.2350	0.0850	0.0650
31	5.0000	3.5000	6.5000	0.2850	0.0550	0.1950	0.2850	0.0550	0.1950
32	5.0000	6.7500	5.2500	0.3375	0.1325	0.1775	0.3375	0.1325	0.1775

To confirm that each of the above variable-node elements satisfies a patch test, a finite element patch as shown in Fig. 3 is tested. As tabulated in Table 1, the exact solution is recovered within the accuracy of the numerical computation. All the elements within this category of the variable-node elements are tested and found to pass the patch test.

3. Adaptive mesh refinement using variable-node elements

Among the key ingredients of the QC is an effective adaptive meshing or refinement scheme that controls the sizes of the individual element subdomains in an adaptive manner, consistent with the severity of deformation. That is, the best use of the present QC method is made when it is combined with automatic adaptive mesh refinement. The adaptive scheme enables one to reach optimal meshing or coarsening so that a high resolution, very often down to the atomic-scale, may be obtained in regions of a stiff gradient of deformation, while appropriate reduction of the degrees of freedom may be accomplished in regions of relatively uniform deformation. Without this process, the mesh must be constructed based only on a priori approximate judgment regarding the deformation behavior, which is scarcely known a priori in many nanomechanics problems. In QC applications for such complex problems, accordingly, an adaptive meshing or refinement scheme is essential for an efficient and accurate solution.

In practice, most of the QC implementations in the literature are limited to linear triangular or tetrahedral elements, as adaptive refinement or meshing is achieved most readily through triangulation for this type of elements, more specifically through the constrained Delaunay triangulation [11]. Note that the variable-node elements discussed in the previous section is capable of bridging the gap between two different scales of meshes smoothly, as reported in finite element methods [15,17,18]. Therefore, the adaptive refinement with the aid of the variable-node elements may be an efficient alternative to the adaptive meshing through the constrained Delaunay triangulation [11] in the conventional QC.

Despite the high geometric adaptability of triangular or tetrahedral elements, these elements are far from being satisfactory in terms of the accuracy and the overall effectiveness. Firstly, tetrahedral elements show poor performance in terms of accuracy, compared with hexahedral elements. Next, the aspect ratios tend to increase for tetrahedral elements as the refinement continues. Elements having large aspect ratios may be found in tetrahedral finite element meshes of complex geometry. In this case, they are usually the source of a substantial error as the nodal points are not appropriate for the sampling points for representing the behaviors of the material points in those element domains. In the same context, the nodal points of a tetrahedral QC element having a large aspect ratio are not suitable for the sampling points to represent the overall deformation behaviors of the atoms contained in the element. To prevent large aspect ratios, in general an adaptive mesh generation code for the constrained Delaunay triangulation is incorporated into the conventional QC with tetrahedral elements. However, the refinement of a mesh of hexahedral elements with the aid of the variable-node elements makes it possible to do without any additional programs for adaptive mesh refinement; no Delaunay triangulation is needed, as opposed to

the QC with tetrahedral elements. In the meantime, it is noteworthy that the aspect ratios of hexahedral elements do not increase in the course of refinement, as will be shown in numerical examples.

In the adaptive refinement method, the mesh keeps track of the deformation magnitude and is increasingly refined according to the severity of the deformation. To estimate the deformations, the deformation measure ε is chosen, as follows [8,30]:

$$\varepsilon = \sqrt{\mathbf{II}(\mathbf{E})}h/a \tag{13}$$

Here, **II**, **E**, h and a denote the second invariant of the strain, the Green strain, the element size and the bond length or the lattice spacing of a domain material, respectively. The strain **E** is simply obtainable according to its definition when the deformation gradient **F** is determined. If an element has a value of ε greater than a given tolerance, the element is refined with nodes being added. Before closing this section, the entire numerical procedure for computation is summarized in the box below.

(1) Read initial data: atom positions $\mathbf{X}_i$ in the reference coordinate, boundary conditions and element data (nodal points and element connectivity).
(2) Make elements data
  (a) Find the element in which an ordinary atom is contained.
  (b) Obtain the shape functions H_α.
(3) Make the clusters and the neighbor lists and calculate cluster weights w^c in Eq. (8).
(4) Minimize the energy E^h_{total} from the cluster summation w.r.t. all nodal points $\mathbf{x}_\alpha$.
(5) Calculate the deformation gradient **F** and the deformation measure ε.
(6) For every element with ε> tolerance, add nodal points on the edge of the element, renew element numbering, connectivity and boundary conditions and go to step 2.
  Else update the positions of atoms and write the data.

4. Numerical examples

In this section, some numerical examples on the nanoindentation simulation are presented to demonstrate the performance of the present QC implementation with variable-node elements. The comparison is made between the two solutions from the conventional QC with tetrahedral elements and from the present QC with variable-node elements. The simulation is carried out for an FCC crystalline structure. The embedded-atom method (EAM) potential, which is widely used for FCC crystals such as Cu, Au, Pt and Al, is chosen. The EAM potential is expressed by the pair potential energy, which is the interaction between atoms and the embedded energy, which is the interaction between an atom and the electronic gas or electronic sea that covers the atom [33,34]. To minimize the system energy, limited-memory BFGS (LBFGS) is chosen [35,36]. LBFGS is popularly adopted when Hessian matrix calculation is not possible and this method employs limited-memory quasi-Newton approximation for the improvement of convergence speed and computing resources.

4.1. Comparison between the present QC with variable-node elements and the conventional QC with tetrahedral elements

In this section, the solution from the new QC with variable-node elements is compared with the solution from the conventional QC with tetrahedral elements to demonstrate the effectiveness of the former. A nanoindentation of a Al (1 1 1) structure is a test problem for this comparison. The EAM potential parameters for Al are listed in Appendix A. The total number of the atoms is 26,297 and the size of the model along the x, y and z directions is 91.6 Å, 79.4 Å and 56.1 Å, respectively. The initial number of representative atoms is 385, which is only 1.5% of the total number of atoms. Fixed boundary condition is applied to the atoms at the bottom along x, y and z directions and the atoms on each of the four lateral faces are fixed in the x and y directions. The initial mesh of tetrahedral elements for the conventional QC is shown in Fig. 4(a), while the initial mesh of variable-node elements for the present QC is shown in Fig. 5(a).

The indenter tip is represented by a repulsive potential, described as follows:

$$E_{ext} = A(R - r_i)^3 \tag{14}$$

Here, the indenter-radius R is set to 10 Å and r_i the distance between the center of the indenter and an atom i. "A" is a constant related to the effective stiffness of the indenter, set to 10 eV/Å^3 in the present simulation.

Fig. 4(a)–(e) show the mesh evolution of the QC with tetrahedral elements according to the adaptive mesh refinement, while Fig. 5(a)–(e) show the mesh evolution of the QC with variable-node elements. In the conventional QC with tetrahedral elements, the constrained Delaunay triangulation code is used with the aid of TetGen [37] for adaptive mesh refinement. Here, the dots indicate the representative atoms. The adaptive meshing criterion ε is chosen to be 0.025 for the QC using

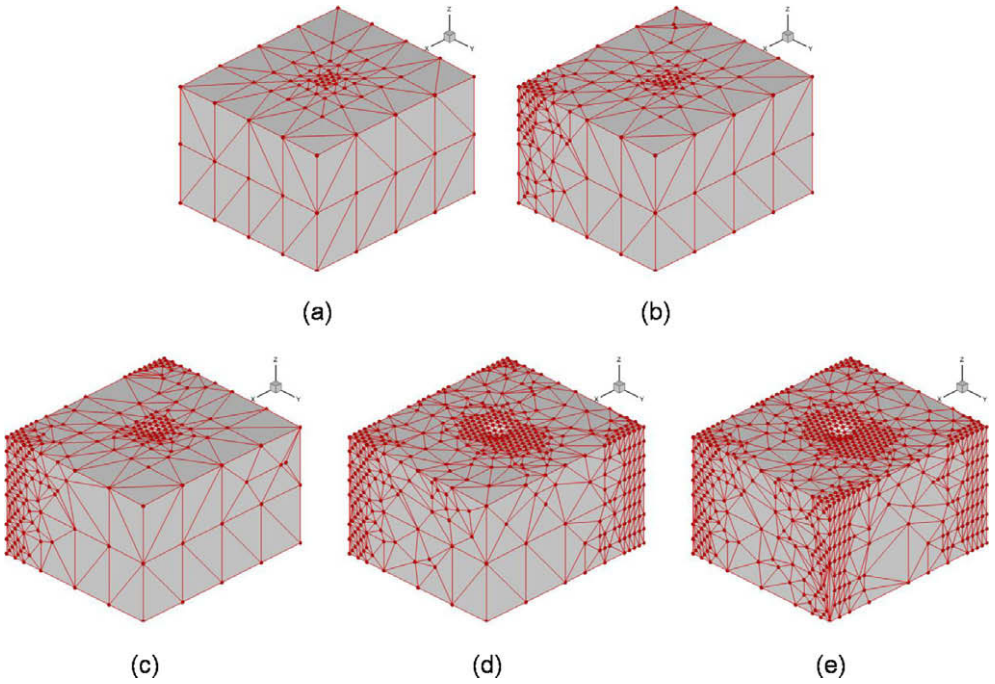

Fig. 4. The mesh evolution in nanoindentation simulation for the QC with tetrahedral elements (the adaptive meshing criterion ε is set to 0.025).

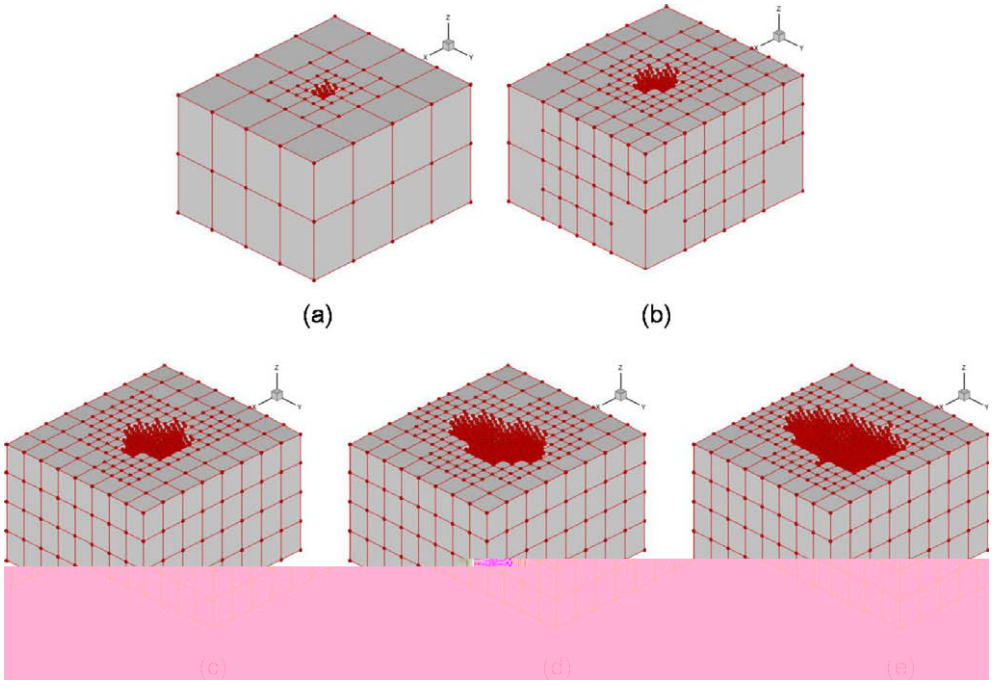

Fig. 5. The mesh evolution in nanoindentation simulation for the QC with variable-node elements (the adaptive meshing criterion ε is set to 0.013).

the tetrahedral mesh and 0.013 for the QC using the variable-node elements. As seen in Table 3, the two cases maintain almost the same degree of accuracy in terms of the normalized root mean square error. As the nanoindentation progresses, high density of representative atoms stands out around the indenting tip on the top surface in both simulations. Note that the aspect ratios of the hexahedral elements in Fig. 5 remain almost uniform throughout the refinement process as the geometric change due to refinement in the mesh is accommodated by various variable-node elements. In contrast, it is hard to

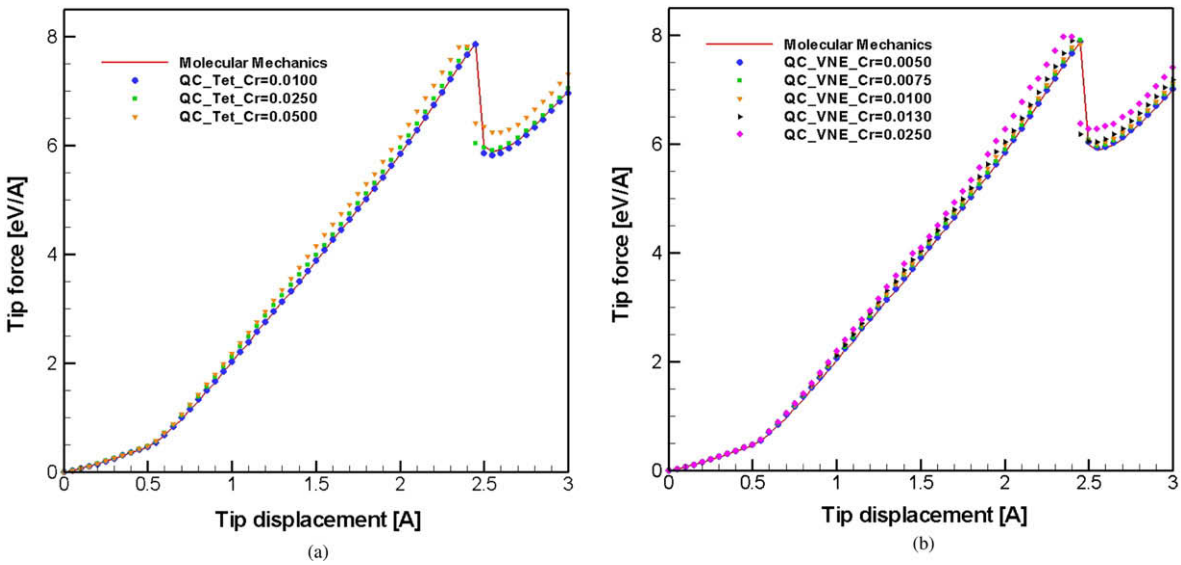

Fig. 6. Load–displacement curves for the nanoindentation simulation; (a) the results from the QC with tetrahedral elements compared with the result from the MM simulation and (b) the results from the QC with variable-node elements compared with the result from the MM simulation.

avoid high aspect ratios for the tetrahedral meshes as shown in Fig. 4 while the refinement is in progress, although the constrained Delaunay triangulation code is utilized.

Three simulations for the conventional QC method are performed to observe the solution behavior while varying the adaptive meshing criterion as 0.0100, 0.0250 and 0.0500. For comparison, five simulations for the present QC method are carried out to observe the solution behavior while varying the adaptive meshing criterion as 0.0050, 0.0075, 0.010, 0.013 and 0.025. A molecular mechanics (MM) simulation is performed to find a reference solution for comparison. The load–displacement curves from the conventional QC with tetrahedral elements and from the QC employing variable-node elements are shown in Fig. 6(a) and (b), respectively. For decreasing values of ε, the solutions from the conventional and from the present QC approach the MM solution. As aforementioned, the meshing criterion $\varepsilon = 0.0250$ for the tetrahedral mesh yields approximately the same accuracy as $\varepsilon = 0.013$ for the variable-node mesh, as shown in Fig. 6(a) and (b) and in Table 3. Comparing these two cases in Table 2, we see that the present QC with variable-node elements needs 3733 representative nodes at the last stage of solution, while the QC with tetrahedral elements uses 3710 representative nodes (see the last column in Table 2). To attain the same degree of accuracy, the two QC methods require almost the same number of the degrees of freedoms in the present nanoindentation problem. In Table 3, the normalized root mean square (NRMS) error norm of tip force between the MM and the QC, the number of iterations for the adaptive mesh refinement and the total time for computation are compared between the two QC methods for $\varepsilon = 0.025$ (tetrahedral mesh) and $\varepsilon = 0.013$ (variable-node element mesh), which yield almost the same accuracy. Note that the QC using variable-node elements requires less iterations for adaptive mesh refinement so that the total time for computation is dramatically shorter than QC with tetrahedral elements. For example, QC using variable-node element with $\varepsilon = 0.013$ eight times faster than the QC with tetrahedral elements with $\varepsilon = 0.0250$ (53 min versus 434 min). The machine used for computing is Intel Core i7 3.2 GHz. The reduction of the computing time is

Table 2
Comparison of the evolving number of representative atoms employed in simulation in the course of the adaptive refinement for various values of ε (QC_Tet: QC with tetrahedral elements; QC_VNE: QC with variable-node elements).

Tip displacement (Å)	0.0	0.5	1.0	1.5	2.0	2.5	3.0
MM	26,297	26,297	26,297	26,297	26,297	26,297	26,297
QC_Tet_Cr = 0.0100	385 (1.5%)	3591 (13.7%)	4373 (16.6%)	5772 (21.9%)	7249 (27.6%)	9399 (35.7%)	10139 (38.6%)
QC_Tet_Cr = 0.0250	385 (1.5%)	390 (1.5%)	1119 (4.3%)	1715 (6.5%)	2181 (8.3%)	2997 (11.4%)	3710 (14.1%)
QC_Tet_Cr = 0.0500	385 (1.5%)	385 (1.5%)	397 (1.5%)	477 (1.8%)	633 (2.4%)	903 (3.4%)	1154 (4.4%)
QC_VNE_Cr = 0.0050	385 (1.5%)	481 (1.8%)	1951 (7.4%)	4700 (17.9%)	9506 (36.1.5%)	11933 (45.4%)	13018 (49.5%)
QC_VNE_Cr = 0.0075	385 (1.5%)	385 (1.5%)	1342 (5.1%)	2670 (10.2%)	4485 (17.1%)	6274 (23.9%)	7182 (27.3%)
QC_VNE_Cr = 0.0100	385 (1.5%)	385 (1.5%)	1043 (4.0%)	1931 (7.3%)	2982 (11.3%)	4601 (17.5%)	5247 (20.0%)
QC_VNE_Cr = 0.0130	385 (1.5%)	385 (1.5%)	947 (3.6%)	1544 (5.9%)	2272 (8.6%)	3262 (12.4%)	3733 (14.2%)
QC_VNE_Cr = 0.0250	385 (1.5%)	385 (1.5%)	385 (1.5%)	947 (3.6%)	1179 (4.5%)	1731 (6.6%)	1974 (7.5%)
QC_VNE_Cr = 0.0500	385 (1.5%)	385 (1.5%)	385 (1.5%)	385 (1.5%)	825 (3.1%)	947 (3.6%)	1057 (4.0%)

Table 3
Comparison of the normalized root mean square(NRMS) error norm, the number of remesh iteration, and computing time employed in simulation in the course of the adaptive refinement for various values of ε (QC_Tet: QC with tetrahedral elements; QC_VNE: QC with variable-node elements). *NRMS error norm* $= \sqrt{\frac{1}{n}\sum_{i=1}^{n}(f_{MM}-f_{QC})^2}/\left(f_{QC}^{\max}-f_{QC}^{\min}\right)$, where f denotes the tip force, and n the total number of sampling points in each load–displacement curve.

Simulation type	NRMS error norm	Remesh interation	Computing time (min)
QC_Tet_Cr = 0.0100	0.0034099	756	459
QC_Tet_Cr = 0.0250	0.0322838	740	434
QC_Tet_Cr = 0.0500	0.0391450	428	275
QC_VNE_Cr = 0.0050	0.0037373	320	61
QC_VNE_Cr = 0.0075	0.0088000	282	56
QC_VNE_Cr = 0.0100	0.0134979	262	54
QC_VNE_Cr = 0.0130	0.0325231	218	53
QC_VNE_Cr = 0.0250	0.0442901	182	45
QC_VNE_Cr = 0.0500	0.0603110	152	49

due to the fact that the QC with variable-node elements is much more efficient than the QC with tetrahedral elements, in reaching to final mesh configuration conforming to the prescribed value of ε. In the finite element method, it is well known that the hexahedral or quadrilateral elements show much faster convergence behavior than the tetrahedral or triangular elements. In addition, the constrained Delaunay triangulation that is used for the QC with tetrahedral elements is not needed for the QC with variable-node elements.

4.2. The performance and efficiency of adaptive mesh refinement

For further detailed investigation of the efficiency and performance of adaptive mesh refinement, a nanoindentation simulation of the Al (1 1 1) direction is carried out using the present QC with variable-node elements and compared with a MM simulation. The total number of atoms is 114,905 and the size of the model along x, y and z directions is 137.5 Å, 119.1 Å and 112.2 Å, respectively. The initial number of the representative atoms is 11,907. The indenter radius is 20 Å and the stiffness parameter A is set to 10 eV/Å^3. The atoms on the bottom are all fixed in the x, y and z *directions* and the atoms on the four lateral faces fixed in the x and y directions. To evaluate the efficiency of the present adaptive mesh refinement scheme, six different simulations are carried out. First, a MM simulation, accounting for every atom, is obtained as a reference solution. Second, QC simulation without adaptive mesh refinement is carried out. The other four simulations are performed to observe the solution behaviors according to the adaptive meshing criterion parameters ε, each of which have four different values: 0.0025, 0.0050, 0.0075 and 0.0100 for ε.

The QC solution without adaptive meshing refinement largely deviates from the MM solution, particularly after the first load drop (see Fig. 7). On the other hand, the QC solutions with adaptive mesh refinement approach the MM solution as the mesh refinement criterion ε is decreased. From Fig. 7, it is seen that the choice of $\varepsilon = 0.005$ yields a solution sufficiently close to the MM solution. As a smaller adaptive meshing criterion is selected, more degrees of freedom are included in

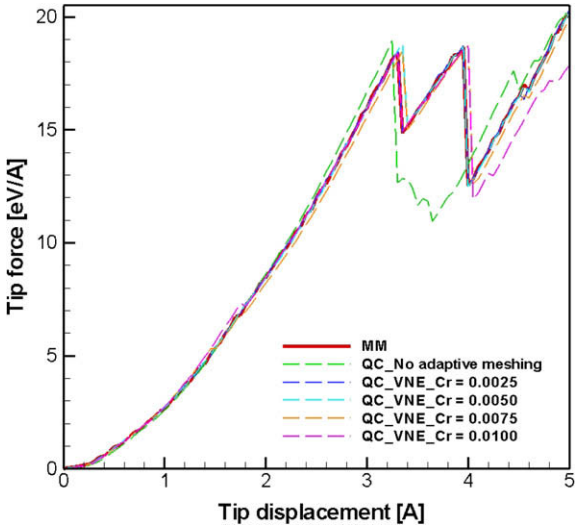

Fig. 7. Load–displacement curves for the nanoindentation simulation; the results from the QC with variable-node elements for various values of ε.

the calculation (see Fig. 8). Through the results in Figs. 7 and 8, the value of ε for adaptive meshing criterion that maintain the accuracy and efficiency of the solution may be determined for the indentation problem.

4.3. Observation of the defects in the simulation of nanoindentation on Al (1 1 1)

To test the present QC method for a large-scale problem, we consider a new nanoindentation simulation on an Al specimen subjected to a tip force on the top surface. The model of the nanoindentation is composed of 2,509,056 Al atoms piled up along the [1 1 1] direction, which is along the z-coordinate. The size of the model in the x, y and z directions is 41.2 nm, 35.7 nm and 28.3 nm, respectively, with the periodic boundary conditions imposed on the four lateral faces (see Fig. 9(a)).

This time the solution from the present QC is compared to the solution from molecular dynamics (MD) simulation, which is widely employed to explore nanoscale material behaviors in material science. The radius of the indenter tip is 5.0 nm and the stiffness parameter A is set to 10 eV/Å^3. The indenting speed is chosen to be 10 m/s. A MD simulation, which considers thermal effect, is essentially different from a QC or a MM simulation based on a molecular static approach. Therefore, the thermal effect is minimized by controlling the temperature at 1 K with a Nose–Hoover thermostat for a proper comparison. The velocity Verlet method is utilized for time integration. The time step is 5fs and the number of simulation steps is 20,000. In addition to the periodic boundary conditions prescribed on the four lateral faces of the body, the free boundary conditions are imposed on the top and the bottom faces. The periodic boundary conditions are employed to reduce the effect of the wave reflection which may influence the defects occurred by nanoindentation and deteriorate the simulation results. Note that we intentionally impose the free boundary condition on the bottom face to prevent the any defects moving downward from bouncing back on the bottom. In addition, uniform counter body force is applied to balance the applied tip force, so that the downward translation of the body due to the applied tip force may be prevented. This technique was used by Li et al. [31] and Lee et al. [23].

The initial model of the QC with variable-node elements is shown in Fig. 9(b). Atoms on the bottom surface are fixed in the x, y and z *directions* and the atoms on the four lateral faces are fixed in the x and y directions, in contrast with the periodic boundary conditions for the MD simulation. The initial number of the representative nodes in the QC model starts with 142,811 representative atoms. In the final stage of simulation, this QC model ends up with 147,252 representative atoms, when ε is chosen to be 0.075.

The load–displacement curves from the MD simulation and from the QC with variable-node elements are shown in Fig. 10. The body undergoes elastic deformation without any defect until the first drop in the load–displacement curve occurs. The initial defect arises upon the first force drop at approximately 5.5 Å and 5.7 Å on the load–displacement curve in QC solution and MD solution, respectively. For the MD simulation, we have applied the periodic BC on the film plane and the free boundary on the bottom with body force to counter the applied loading on the top. This is different from the boundary conditions in the QC case, in which no wave effects appear. In the MD model all reflected stress waves from the free surface on the bottom have the opposite sign of the incoming waves, so that the wave effects are minimal. Therefore, the same response is expected between the MD and the QC within elastic response despite the difference in boundary conditions. However, the two solutions come out different once plasticity is developed or defects are generated as the displacement depends on the defect behaviors including dislocation glides and the defects are developed in different ways between the MD model and the QC model due to different loading rates and boundary conditions.

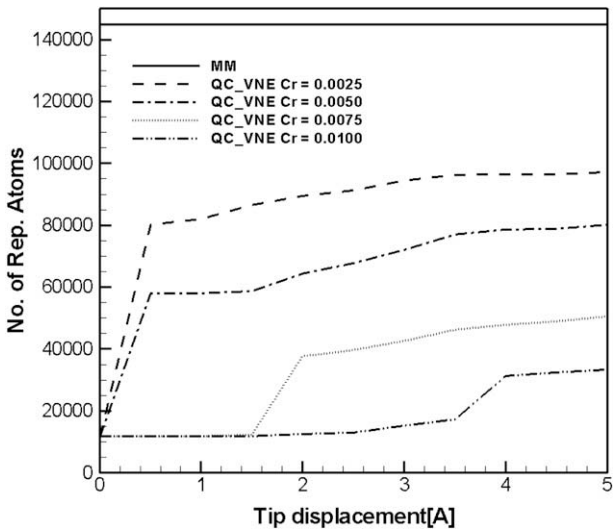

Fig. 8. Increasing numbers of the representative atoms versus the tip displacement for various values of ε.

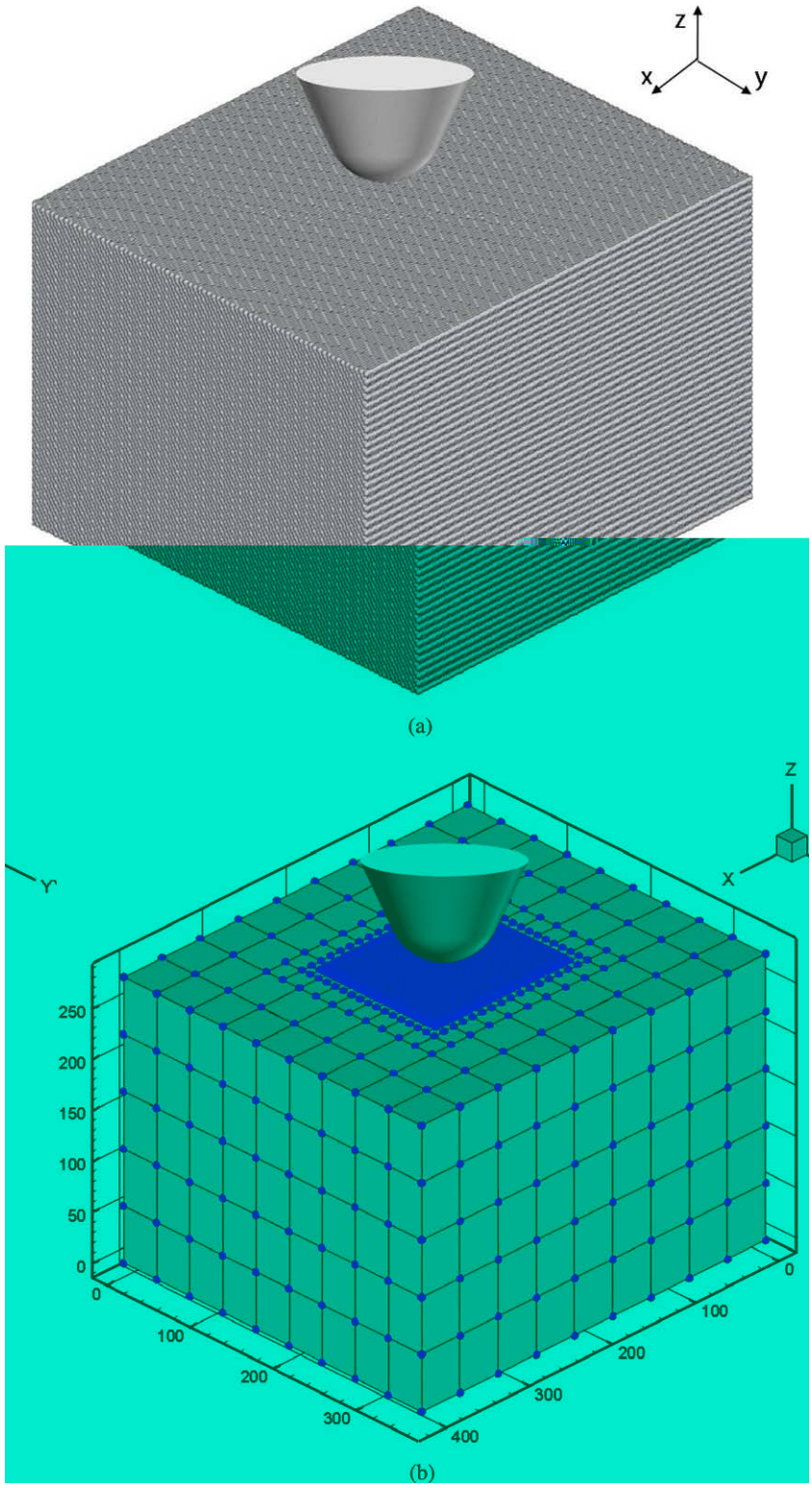

Fig. 9. An initial model for the nanoindentation simulation of an Al(111) structure; (a) A model for MD simulation with the number of the atoms being 2,509,056 and (b) A model for QC using variable-node elements with the number of the representative atoms being 142,811.

Fig. 11(a) and (b) shows the initial defect formation from the MD and the QC simulation. Both of them show the well known embryonic dislocation that is developed from the site of homogeneous nucleation (see ref.[23]). Note that all interior

atoms away from defects have been removed in Fig. 11(a) and (b), utilizing the centrosymmetry parameter [38]. An embryonic dislocation takes place in the two planes of $(\bar{1}\,1\,1)$ and $(1\,\bar{1}\,1)$ among the $\{1\,1\,1\}$ slip planes (see Fig. 11(c)). This phenomenon has been observed and presented by a number of researchers [23,31]. In the subsequent stage, the embryonic defect is developed into the well known tetrahedral lock (see [23]). Note that the embryonic dislocation is also observed in the QC simulation along the same slip planes. Note that the load–displacement curves from the MD simulation and the QC simulation are close to each other up to the point of the first load drop and that both simulations predict the formation of the same initial defects.

4.4. Nanoindentation simulations on the (1 1 1) surface of an Al nanostructure containing a void

In this section, the variations in the mechanical behaviors induced by the defect of a void are explored. For this we again consider a nanoindentation on Al (1 1 1) nanostructure. The size of the simulation models along the x, y and z directions is 137.5 Å, 119.1 Å and 112.2 Å, respectively. This model consists of 114,905 Al atoms piled up in the [1 1 1] direction, which is along the z-coordinate. The number of representative atoms is 13,586. The radius of the indenter tip is 20 Å and the stiffness parameter A is set to 10 eV/Å^3. Atoms on the bottom are fixed along the x, y and z directions, and the atoms on the four sides are fixed in the x and y directions.

First, six nanoindentation simulations are carried out. The first model does not have a void inside the body, while the other five models have a void with a radius of 15 Å. The void in the body is located at the center of the x–y plane and the position of the void center along the z direction is varied: 0.5 × height of the specimen, 0.6 × height, 0.7 × height, 0.8 × height and 0.9 × height. The load–displacement curves for these simulations are shown in Fig. 12. Throughout the simulations, as the void approaches the top free surface, the slope of the curve tends to decrease as the resistance to the downward displacement of the tip is reduced with the increasing heights of the void. When the height of the void is 0.8 × height, the slope of the curve and the tip force are reduced drastically. For the 0.9 × height case, the void is not completely embedded inside the body, but its upper part is exposed out on the top surface of the body, forming a hole on the top surface. The indenter tip starts to interact with the body at the tip displacement of 4 Å. However, while the distance of the void from the bottom increases up to the 0.7 × height, the maximum tip force continues to increase gradually in proportion to this distance, with the increasing delay in the first load drop. To confirm these characteristics, the defect configurations inside the body are visualized using the centrosymmetry parameter and a comparison is made for various void heights: 0.5 × height, 0.7 × height, and 0.8 × height and for the case without a void (see Figs. 13–16). In Figs. 13–16, we employed the visualization technique of centrosymmetry parameter that has successfully proven effective for the studies of dislocation nucleation in fcc crystals [23,38]. Every atom in perfect fcc single crystal has twelve nearest-neighboring atoms. For one atom, each of its neighbors can be paired with an opposite nearest neighbor. The centrosymmetry parameter P for this atom is then defined as

$$P = \sum_{i=1}^{6} |\mathbf{R}_i - \mathbf{R}_{i+6}|^2 \tag{15}$$

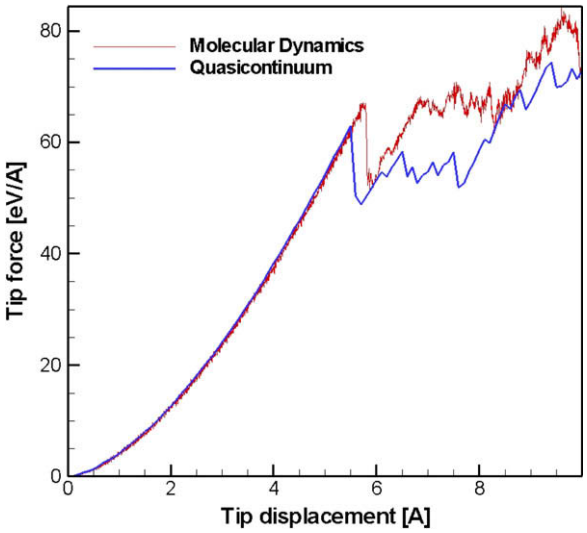

Fig. 10. Comparison in the load–displacement curves between the QC and the MD simulation; the blue line and the red line indicate the results of QC and MD, respectively. The first drop points where the embryonic dislocation occurs are at 5.5 Å and 5.7 Å in the cases of QC and MD, respectively.

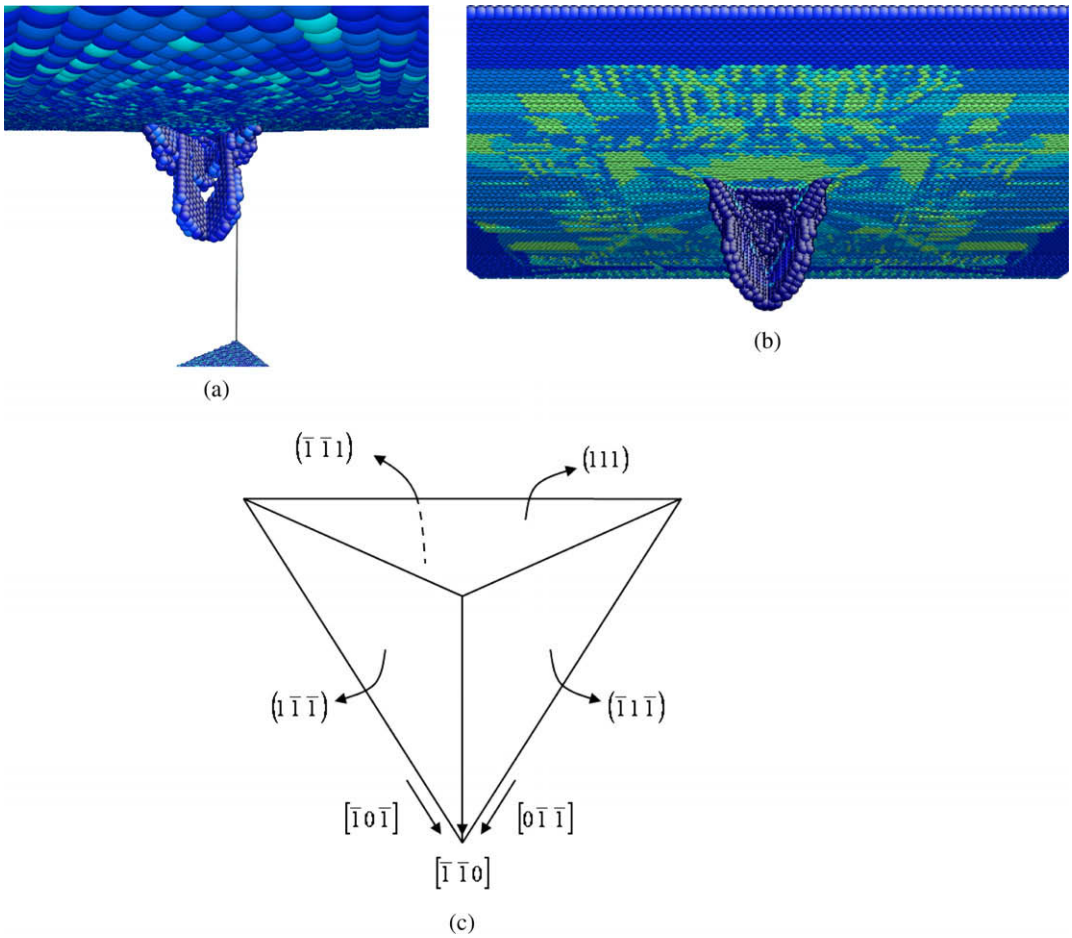

Fig. 11. A defect is produced in nanoindentation simulation; (a) The configuration of embryonic dislocation from the MD simulation, (b) The configuration of embryonic dislocation from the QC simulation and (c) The slip system of the fcc {1 1 1} surface.

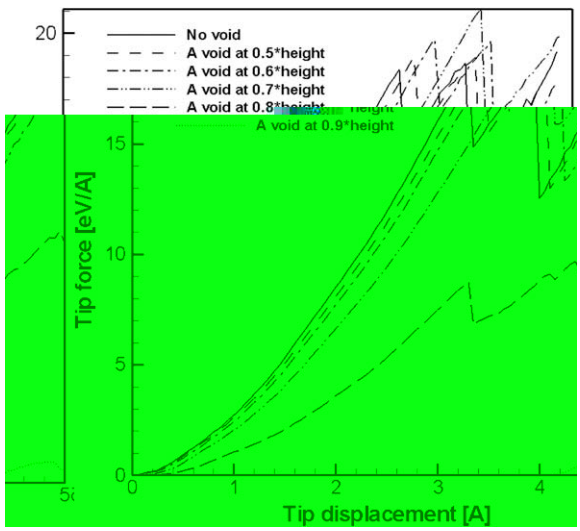

Fig. 12. Load–displacement curves for the nanoindentation simulation for varying heights of a void center.

where the $\mathbf{R}_i$ and $\mathbf{R}_{i+6}$ together stand for the six pairs. The parameter therefore vanishes for each atom that rests at the site of perfect fcc lattice structure. If there exists a defect such as vacancy and dislocation, the parameter for an atom in the vicinity

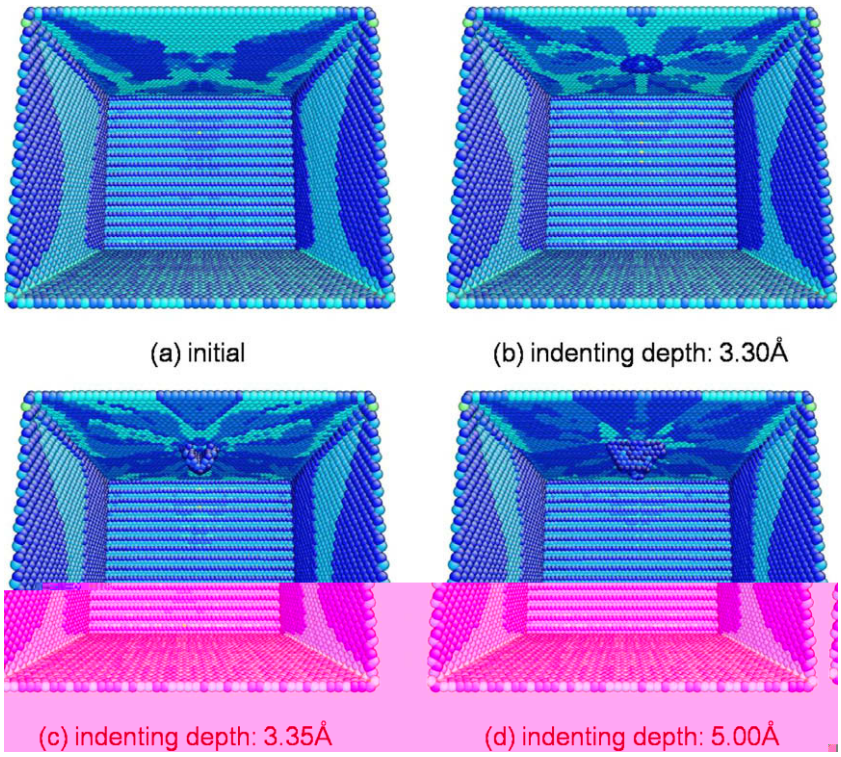

Fig. 13. Snapshots of nanoindentation simulation in terms of the centrosymmetry parameter for the case of no void.

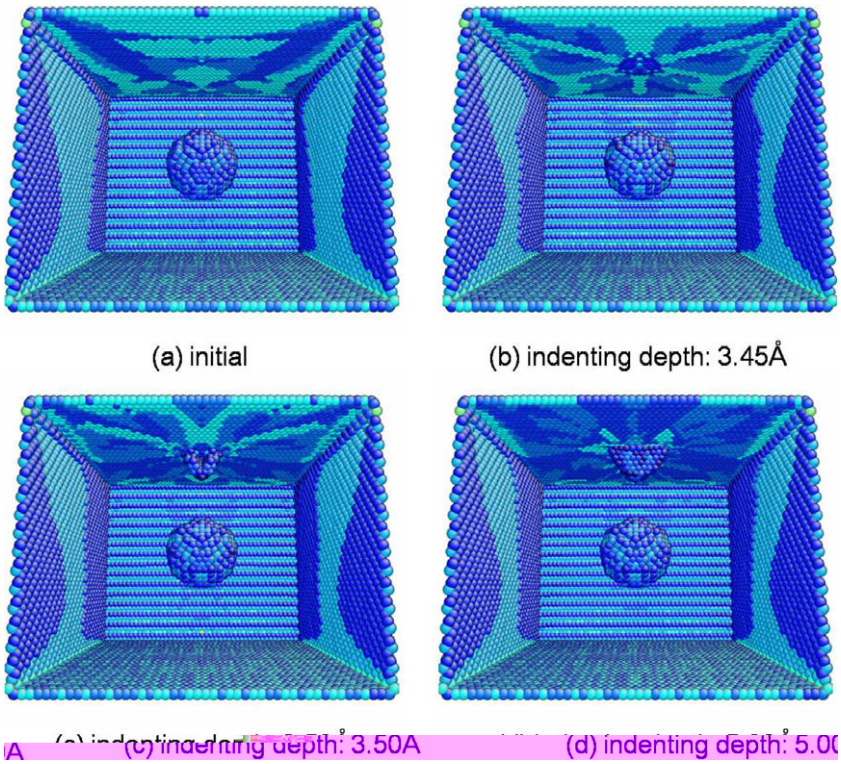

Fig. 14. Snapshots of nanoindentation simulation in terms of the centrosymmetry parameter for the case of a void center at 0.6 × height.

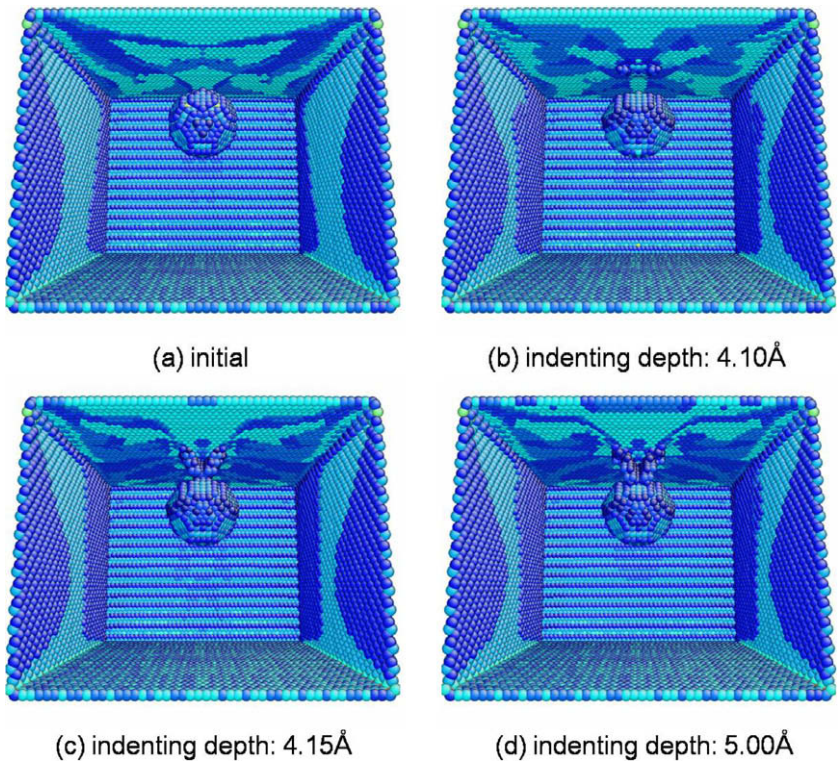

Fig. 15. Snapshots of nanoindentation simulation in terms of the centrosymmetry parameter for the case of a void center at 0.7 × height.

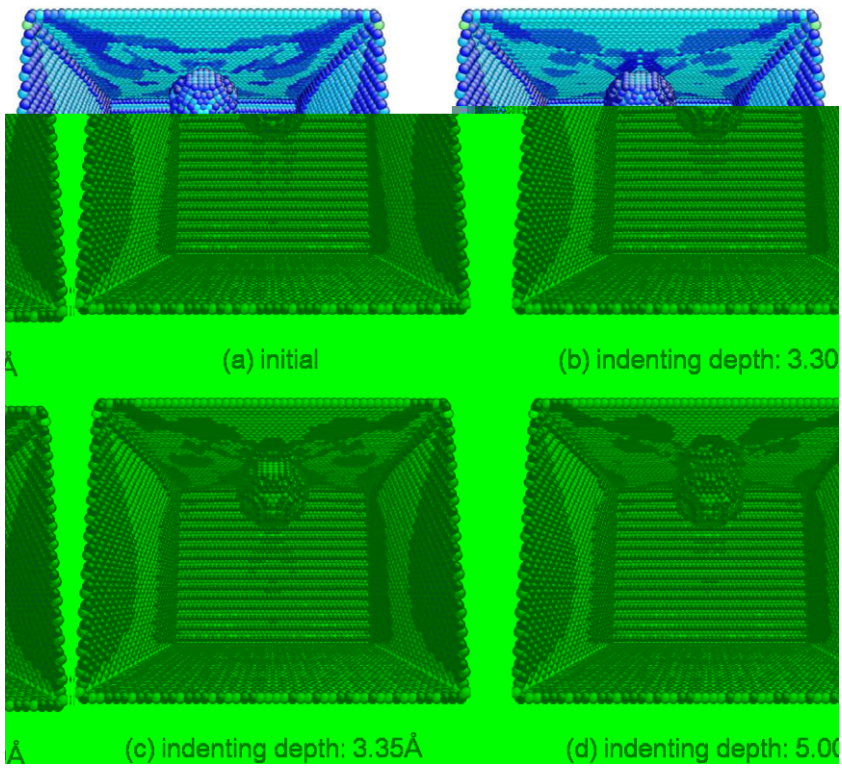

Fig. 16. Snapshots of nanoindentation simulation in terms of the centrosymmetry parameter for the case of a void center at 0.8 × height.

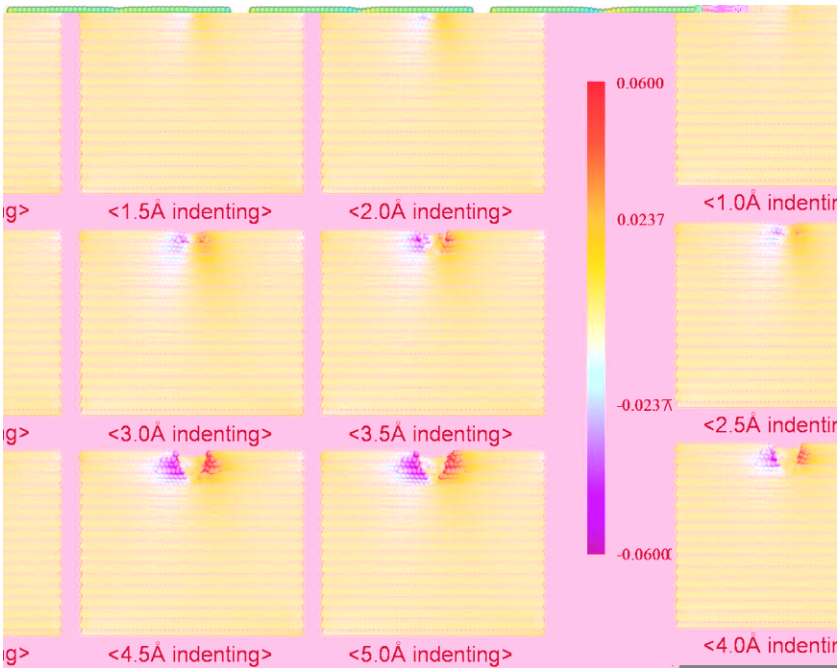

Fig. 17. Shear strain ε_{13} plots from the nanoindentation simulation for the case of no void.

of the defect has some finite magnitude. When its magnitude is less than a cutoff value, we eliminated the corresponding atom from visualizing our simulation results. Therefore, only defect-related atoms are visible. Thinner color tone indicates a relatively larger value of the centrosymmetry parameter, which implies more distortion of the lattice.

Apart from the 0.8 $\times$ height case, the embryonic dislocation in Fig. 13(c) emerges upon the first drop of the load–displacement curve, and the tetrahedral lock in Fig. 13(d) occurs at the second drop point (see Fig. 12). However, when the void is located at 0.8 $\times$ height from the bottom, the defects and the voids meet with each other, and a distinct second load drop does

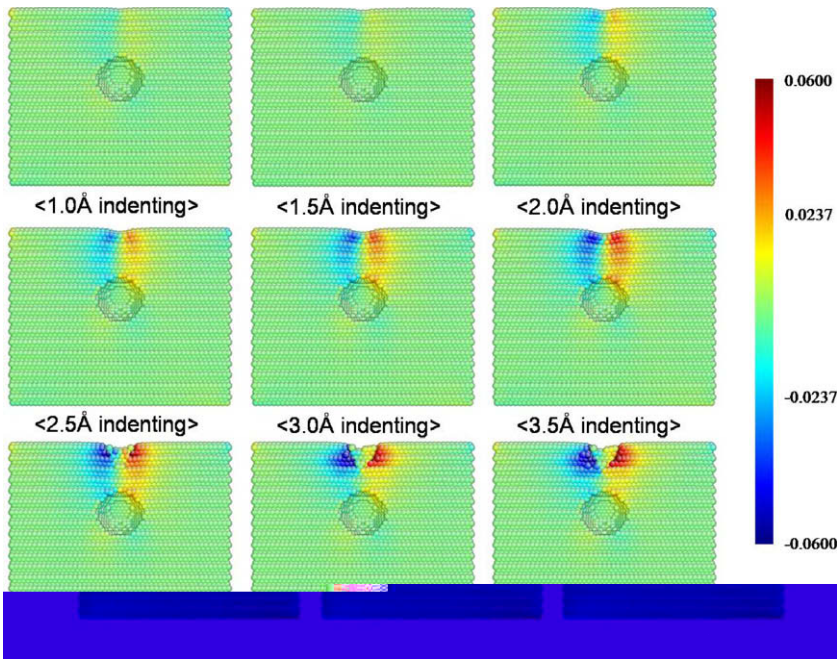

Fig. 18. Shear strain ε_{13} plots from the nanoindentation simulation for the case of a void center at 0.6 $\times$ height.

not appear (see Fig. 12). Atomic level strain (ε_{13}) is calculated for the four cases; no void, 0.6 × height, 0.7 × height and 0.8 × height (see Figs. 17–20). After the first drop, high strains occur along with the slip planes for every case. In the case of no void, the embryo is generated, accompanying only a little amount of strain. In contrast, in the case of 0.6 × height and 0.7 × height, relatively high strain field is created on the atoms located between the contact area of the indenter and the void. Finally, for the case of 0.8 × height, high local strain field starts to build up around the top of the void in the early stage of indentation.

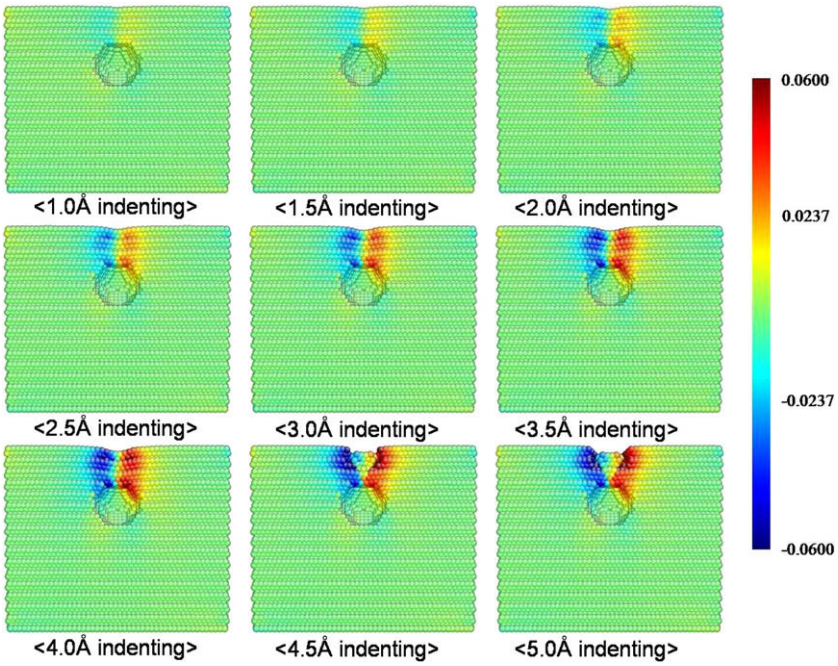

Fig. 19. Shear strain ε_{13} plots from the nanoindentation simulation for the case of a void center at 0.7 × height.

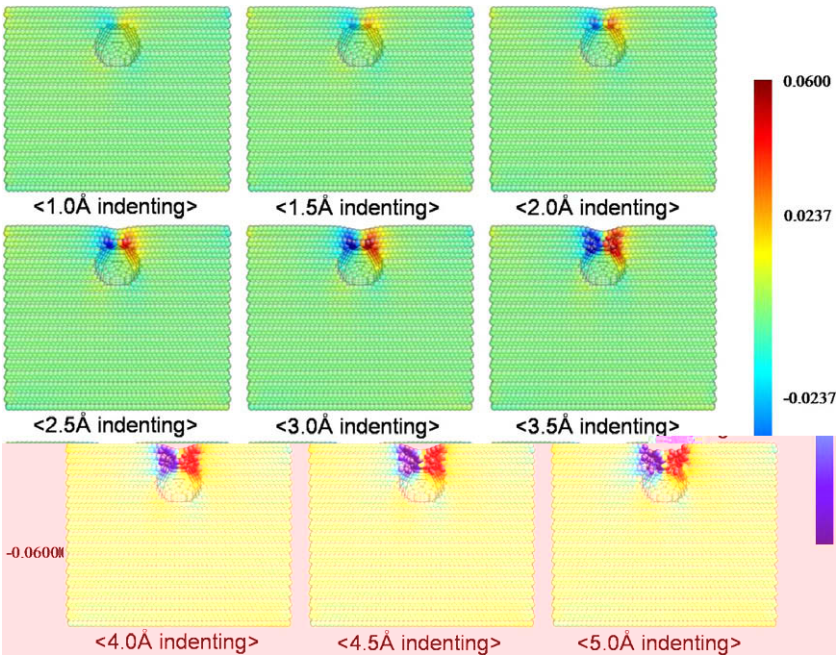

Fig. 20. Shear strain ε_{13} plots from the nanoindentation simulation for the case of a void at 0.8 × height.

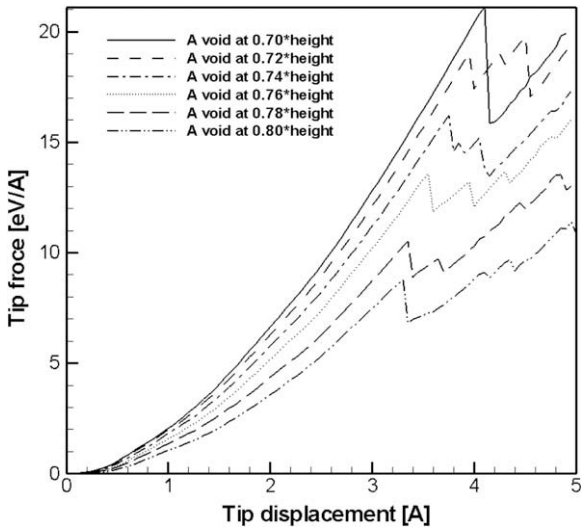

Fig. 21. Load–displacement curves from the nanoindentation simulation for varying heights of a void center from 0.70 × height to 0.80 × height.

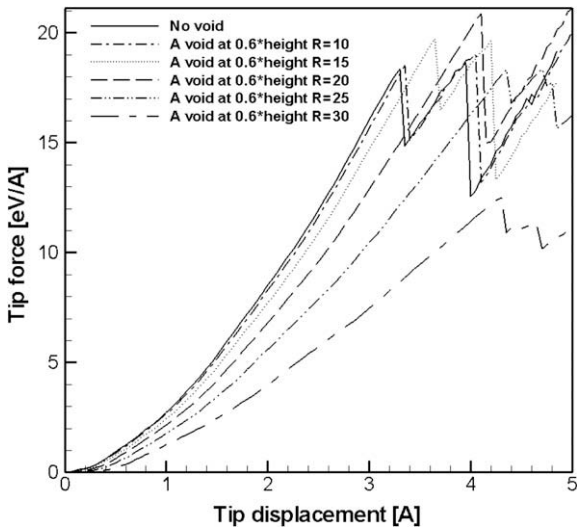

Fig. 22. Load–displacement curves from the nanoindentation simulation for various radii of the void.

To look into the detailed behavior according to the void heights, the increment of the void height is further reduced between the two cases of the 0.7 × height and 0.8 × height. As shown in Fig. 21, when the position of the void exceeds the 0.7 × height case, the tip force and the first drop point tend to decrease and the maximum tip force is found to be between the height of 0.69 and 0.70.

Next, the load–displacement curves are compared for various radii of the void from 10 Å to 30 Å while fixing the location of the void to be 0.6 × height. As shown in Fig. 22, the tip force continues to increase and the first drop is delayed for increasing radii R = 10 Å, 15 Å, 20 Å, 25 Å and 30 Å. Note that the maximum tip force is produced for the case of R = 20 Å. This means that for a fixed location of the void center there is a definite size of the radius that leads to the maximum load sustained by the body before the first load drop takes place in the nanoindentation.

5. Conclusion

In the present work, we propose a new simple QC method using the variable-node elements. The advantage of the proposed QC may summarized as

(i) No adaptive meshing code for the constrained Delaunay triangulation is needed, but only the coding of the explicit shape function is needed. Therefore, the coding of this QC method is straightforward.
(ii) In the course of adaptive refinement, the aspect ratios of the refined elements are maintained almost uniform, in contrast with the occurrence of large aspect ratios for the tetrahedral elements used in the conventional QC.
(iii) The proposed QC shows more rapid convergent behavior than the conventional QC, as verified by the fact that only 1/3 of the iterations needed for the conventional QC is required for the present QC to maintain the same accuracy in the nanoindentation problem chosen.
(iv) The total computing time is drastically reduced in the present QC method than in the conventional QC method, as verified by the example of the nanoindentation problem chosen.

Some numerical examples on the nanoindentation have been presented to demonstrate the effectiveness of the proposed QC method. In passing, we state that QC simulations on systems containing a larger number of atoms are under investigation to explore the effects of the internal defects, like voids or impurities, on material properties through nanoindentation. In addition, lattice systems other than FCC will be treated in this study. This will be reported in the subsequent paper in the future.

Acknowledgments

This research was supported through NRL (National Research Lab) program by the Korea Science and Engineering Foundation funded by the Ministry of Education, Science and Technology (R0A-2007-000-20115-0), through National Nuclear Technology Program by Korea Institute of Science & Technology Evaluation and Planning (KISTEP) and the Ministry of Education, Science and Technology, Korean Government, and through Grant 08k1401-00611 by Center for Nanoscale Mechatronics& Manufacturing, one of the 21st Century Frontier Research Programs, which are supported by Ministry of Education, Science and Technology, Korea.

Appendix A. EAM potential parameters

The EAM is widely employed to describe system crystalline metals. The potential energy of metal atoms is described by the pair potential of the two-body interaction and the embedded energy caused by the electron sea or gas around the atom.

$$E_{total} = \sum_i F_i(\rho_i) + \sum_{i>j} \varphi(r_{ij}) \tag{A.1}$$

$$\rho_i = \sum_{j(j\neq i)} f(r_{ji}) \tag{A.2}$$

Here, φ, r_{ij}, and F_i are the pair potential, the distance between atom i and atom j, and the embedded energy defined by the electron density ρ_i, respectively. The electron density of atom i is obtained by the summation of the electron density $f(r_{ij})$ over every individual atom j. The EAM potential was initially proposed by Daw and Baskes [33]. In the present work, the pair potential and the embedded energy proposed by Cai and Ye [34] have been chosen. This is described as shown below.

$$F_i(\rho_i) = -F_0\left[1 - \ln\left(\frac{\rho_i}{\rho_e}\right)^n\right]\left(\frac{\rho_i}{\rho_e}\right)^n + F_1\left(\frac{\rho_i}{\rho_e}\right) \tag{A.3}$$

$$(f(r_{ij}) = f_e \exp\left[-\chi(r_{ij} - r_e)\right] \tag{A.4}$$

$$\varphi(r_{ij}) = -\alpha\left[1 + \beta(r_{ij}/r_a - 1)\right]\exp\left[-\beta(r_{ij}/r_a - 1)\right] \tag{A.5}$$

Cai employed a cutoff radius of $1.65 \times a_0$ to correct every variable [34]. Here, a_0 is the lattice constant. For aluminum, the lattice constant is 4.05 Å; the parameters are described as follows.

$$F_0 = 2.61\ \text{eV},\quad \rho_e = 12.449,\quad n = 0.5,\quad F_1 = -0.1392\ \text{eV},\quad \beta = 7.5995,\quad f_e = 1.0,\quad r_e = 2.8638,\quad \chi = 2.5\ \text{Å},$$
$$r_a = 3.0169\ \text{Å},\quad \alpha = 0.0834\ \text{eV}$$

References

[1] D. Passerone, M. Parrinello, Action-derived molecular dynamics in the study of rare events, Phys. Rev. Lett. 87 (2001) 108302–108305.
[2] I.-H. Lee, J. Lee, S. Lee, Kinetic energy control in action-derived molecular dynamics simulations, Phys. Rev. B 68 (2003) 64303–64310.
[3] G. Mills, H. Jonsson, Quantum and thermal effects in H2 dissociative adsorption: evaluation of free energy barriers in multidimensional quantum systems, Phys. Rev. Lett. 72 (1994) 1124–1127.
[4] S. Tang, T.Y. Hou, W.K. Liu, A pseudo-spectral multiscale method: interfacial conditions and coarse grid equations, J. Comput. Phys. 213 (2006) 57–85.
[5] E.B. Tadmor, M. Ortiz, R. Philips, Quasicontinuum analysis of defects in solids, Philos. Mag. A 73 (1996) 1529–1563.
[6] R.E. Miller, E.B. Tadmor, The quasicontinuum method: overview, applications and current directions, J. Computer-Aided Mater. Design 9 (2002) 203–239.
[7] V.B. Shenoy, R. Miller, E.B. Tadmor, D. Rodney, R. Philips, M. Ortiz, Nucleation of dislocations beneath a plane strain indenter, J. Mech. Phys. Solids 48 (2000) 649–673.
[8] J. Knap, M. Ortiz, An analysis of the quasicontinuum method, J. Mech. Phys. Solids 49 (2001) 1899–1923.

[9] J.Y. Park, S. Im, An adaptive nonlocal quasicontinuum for deformations of curved crystalline structures, Phys. Rev. B 77 (2008) 184109.
[10] V.B. Shenoy, R. Miller, E.B. Tadmor, R. Phillips, M. Ortiz, An adaptive finite element approach to atomic-scale mechanics – the quasicontinuum method, J. Mech. Phys. Solids 47 (1998) 611–642.
[11] D.T. Lee, B.J. Schachter, Two algorithms for constructing a Delaunay triangulation, Int. J. Comput. Inform. Sci. 9 (1980) 219–242.
[12] Y.-S. Cho, S. Im, MLS-based variable-node elements compatible with quadratic interpolation. Part I: Formulation and application for non-matching meshes, Int. J. Numer. Methods Eng. 65 (2006) 494–516.
[13] Y.-S. Cho, S. Jun, S. Im, H.-G. Kim, An improved interface element with variable nodes for non-matching finite element meshes, Comput. Methods Appl. Mech. Eng. 194 (2005) 3022–3046.
[14] J.H. Lim, S. Im, Y.-S. Cho, Variable-node finite elements for non-matching meshes by means of MLS (Moving Least Square) scheme, Int. J. Numer. Methods Eng. 72 (2007) 858–882.
[15] J.H. Lim, S. Im, Y.-S. Cho, MLS (Moving Least Square)-based finite elements for three-dimensional non-matching meshes and adaptive mesh refinement, Comput. Methods Appl. Mech. Eng. 196 (2007) 2216–2228.
[16] J.H. Kim, J.H. Lim, J.H. Lee, S. Im, A new computational approach to contact mechanics using variable-node finite elements, Int. J. Numer. Methods Eng. 73 (2008) 1966–1988.
[17] J.H. Lim, S. Im, (4+n)-noded MLS (Moving Least Square)-based finite elements for mesh gradation, Struct. Eng. Mech. 25 (2007) 91–106.
[18] C.-K. Choi, N.-H. Lee, A 3-D adaptive mesh refinement using variable-node solid transition elements, Int. J. Numer. Methods Eng. 39 (1996) 1585–1606.
[19] A.C. Fischer-Cripps, Nanoindentation, Springer-Verlag, 2002.
[20] R.W. Carpick, M. Salmeron, Scratching the surface: fundamental investigations of tribology with atomic force microscopy, Chem. Rev. 97 (1997) 1163–1194.
[21] R. Komanduri, N. Chandrasekaran, L.M. Raff, MD simulation of indentation and scratching of single crystal aluminum, Wear 240 (2000) 113–143.
[22] S. Jun, Y. Lee, S.Y. Kim, S. Im, Large-scale molecular dynamics simulations of Al(1 1 1) nanoscratching, Nanotechnology 15 (2004) 1169–1174.
[23] Y. Lee, J.Y. Park, S.Y. Kim, S. Jun, S. Im, Atomistic simulations of incipient plasticity under Al(1 1 1) nanoindentation, Mech. Mater. 37 (2005) 1035–1048.
[24] E.T. Lilleodden, J.A. Zimmerman, S.M. Foiles, W.D. Nix, Atomistic simulations of elastic deformation and dislocation nucleation during nanoindentation, J. Mech. Phys. Solids 51 (2003) 901–920.
[25] D. Feichtinger, P.M. Derlet, H. Van Swygenhoven, Atomistic simulations of spherical indentations in nanocrystalline gold, Phys. Rev. B 67 (2003) 024113.
[26] X. Ma, W. Yang, Molecular dynamics simulation on burst and arrest of stacking faults in nanocrystalline Cu under nanoindentation, Nanotechnology 14 (2003) 1208–1215.
[27] G.S. Smith, E.B. Tadmor, N. Bernstein, E. Kaxiras, Multiscale simulations of silicon nanoindentation, Acta Mater. 49 (2001) 4089–4101.
[28] R.C. Picu, Atomistic-continuum simulation of nano-indentation in molybdenum, J. Computer-Aided Mater. Design 7 (2000) 77–87.
[29] D. Shan, L. Yuan, B. Guo, Multiscale simulation of surface step effects on nanoindentation, Mat. Sci. Eng. A 412 (2005) 264–270.
[30] J. Knap, M. Ortiz, Effect of indenter-radius size on Au(0 0 1) nanoindentation, Phys. Rev. Lett. 90 (2003) 226102.
[31] J. Li, K.J. Van Vliet, T. Zhu, S. Yip, S. Suresh, Atomistic mechanics governing elastic limit and incipient plasticity in crystals, Nature 418 (2002) 307–310.
[32] T.J.R. Hughes, The Finite Element Method, Prentice Hall, New Jersey, 1987.
[33] M.S. Daw, M.I. Baskes, Embedded-atom method: derivation and application to impurities, surfaces, and other defects in metals, Phys. Rev. B 29 (1984) 6443–6453.
[34] J. Cai, Y.Y. Ye, Simple analytical embedded-atom-potential model including a long-range force for fcc metals and their alloys, Phys. Rev. B 54 (1996) 8398–8412.
[35] J. Nocedal, Updating quasi-Newton matrices with limited storage, Math. Comput. 24 (1980) 773–782.
[36] D.C. Liu, J. Nocedal, On the limited memory BFGS method for large scale optimization, Math. Program. 45 (1989) 503–528.
[37] H. Si, TetGen, A Quality Tetrahedral Mesh Generator and Three-Dimensional Delaunay Triangulator, 2007. This code is linked, <http://tetgen.berlios.de/>.
[38] C.L. Kelchner, S.J. Plimpton, J.C. Hamilton, Dislocation nucleation and defect structure during surface indentation, J. Phys. Rev. B 58 (1998) 11085–11088.